Geophysical Journal International

Geophys. J. Int. (2021) **224,** 581–589
Advance Access publication 2020 August 17
GJI Seismology

doi: 10.1093/gji/ggaa386

The earthquake arrest zone

Chun-Yu Ke [1], Gregory C. McLaskey[1] and David S. Kammer [2]

[1] *School of Civil and Environmental Engineering, Cornell University, Ithaca, NY 14850, USA*
[2] *Institute for Building Materials, ETH, Zürich, Switzerland. E-mail: dkammer@ethz.ch*

Accepted 2020 August 10. Received 2020 August 6; in original form 2019 October 25

SUMMARY

Earthquake ruptures are generally considered to be cracks that propagate as fracture or frictional slip on pre-existing faults. Crack models have been used to describe the spatial distribution of fault offset and the associated static stress changes along a fault, and have implications for friction evolution and the underlying physics of rupture processes. However, field measurements that could help refine idealized crack models are rare. Here, we describe large-scale laboratory earthquake experiments, where all rupture processes were contained within a 3-m long saw-cut granite fault, and we propose an analytical crack model that fits our measurements. Similar to natural earthquakes, laboratory measurements show coseismic slip that gradually tapers near the rupture tips. Measured stress changes show roughly constant stress drop in the centre of the ruptured region, a maximum stress increase near the rupture tips and a smooth transition in between, in a region we describe as the earthquake arrest zone. The proposed model generalizes the widely used elliptical crack model by adding gradually tapered slip at the ends of the rupture. Different from the cohesive zone described by fracture mechanics, we propose that the transition in stress changes and the corresponding linear taper observed in the earthquake arrest zone are the result of rupture termination conditions primarily controlled by the initial stress distribution. It is the heterogeneous initial stress distribution that controls the arrest of laboratory earthquakes, and the features of static stress changes. We also performed dynamic rupture simulations that confirm how arrest conditions can affect slip taper and static stress changes. If applicable to larger natural earthquakes, this distinction between an earthquake arrest zone (that depends on stress conditions) and a cohesive zone (that depends primarily on strength evolution) has important implications for how seismic observations of earthquake fracture energy should be interpreted.

Key words: Friction; Spatial analysis; Mechanics, theory, and modelling.

1 INTRODUCTION

The slip profile of an earthquake rupture is the spatial distribution of displacement discontinuity between the fault surfaces, $\delta(x)$. The slip profile of a single earthquake is directly related to the spatial distribution of on-fault stress changes associated with the rupture, $\Delta\tau(x)$. It is therefore important for understanding the mechanics of earthquakes and has implications for stress drop, stress redistribution and earthquake-to-earthquake triggering (Freed 2005).

Most analytical models of slip profiles are mathematically convenient but can produce physically unrealistic results. Earthquakes are commonly modelled as shear cracks, and the linear elastic crack model (Bilby & Eshelby 1968) established that a perfect crack with uniform shear stress drop within the rupture area leads to an elliptical slip profile (Fig. 1a). This 'elliptical model' casts an infinite stress increase at the rupture tips, which is unrealistic because real interfaces have finite strength. Cowie & Scholz (1992) and Bürgmann *et al.* (1994) assumed perfectly plastic failure near the rupture tips by adapting the Dudgale (1960) model to a mode II crack. The resulting 'bell-shaped' model, shown in Fig. 1(a), assumes a constant stress drop inside the ruptured region and a constant stress increase near the rupture tips (Fig. 1c). However, in our experiments, we did not observe a constant stress increase near the rupture tips.

Most past field studies of fault slip distributions provide information relevant to the growth of brittle faults over many earthquakes or slow slip events. Studies of faulting showed that slip gradients appeared approximately constant near the fault tip (Muraoka & Kamata 1983; Walsh & Watterson 1987; Dawers *et al.* 1993; Nicol *et al.* 1996; Manighetti *et al.* 2001), typically 20 per cent of the rupture length (Cowie & Scholz 1992; Scholz & Lawler 2004). When considering slip profiles from individual events, measured slip distributions are often so heterogeneous that stacking of many individual events is required to evaluate features. Using this approach, Manighetti *et al.* (2005) found that slip distributions derived from kinematic models and field observations were roughly triangular

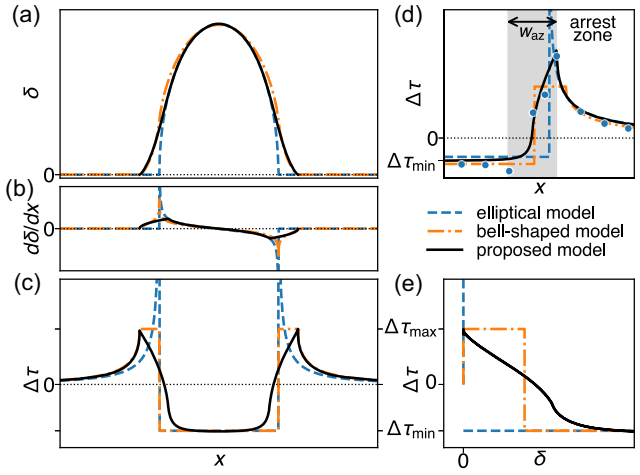

Figure 1. Examples of (a) slip profile $\delta(x)$, (b) first derivative of slip profile $d\delta(x)/dx$ and (c) associated shear stress changes $\Delta\tau(x)$. The bell-shaped model is designed to limit the maximum shear stress, casting a constant $\Delta\tau$ plateau near rupture tips under uniform loading and strength field. The proposed model preserves the elliptical slip profile in the centre and swaps the edges of the crack with $x^{3/2}$ form, eliminates shear stress singularities, keeps $\Delta\tau(x)$ peaks at rupture tips, and produces a smooth distribution of stress changes with the earthquake arrest zone. (d) A zoom-in of (c) shows the earthquake arrest zone (shaded) in more detail and presents example laboratory measurements (blue dots) of near-fault stress changes with fitted models. w_{az} denotes earthquake arrest zone width. Two distinct data measurements lie inside the earthquake arrest zone where stress changes transition from an apparent maximum level, $\Delta\tau_{max}$, at the crack tip to a minimum level, $\Delta\tau_{min}$, inside the crack. (e) Illustration of the earthquake stress change versus slip, $\Delta\tau$–δ, relationship of all three models.

and predominantly asymmetric. Walsh & Watterson (1987) argued that the ubiquitous linear tapering feature of slip profiles can be the result of cumulative slips from multiple growing cracks with elliptical shape. This argument highlights the difficulty of distinguishing the field measurements of slip profiles accumulated across multiple earthquake ruptures and of a single earthquake rupture, which will result in very different shapes and possibly different conclusions.

Slip at the rupture tips is small and difficult to measure, but can have a strong influence on stress changes. In this work, we use measurements of laboratory earthquakes to illuminate the features of earthquake slip profiles, including the area near the rupture tip. We present results from recent large-scale laboratory experiments where the rupture processes are partially or completely contained in a 3-m long saw-cut granite fault (Ke *et al.* 2018; McLaskey 2019; Wu & McLaskey 2019). This provides a unique opportunity to measure local slip and local static shear stress changes near the tip of an arrested rupture. Similar to observations from natural fault ruptures, we consistently observe slip profiles that taper approximately linearly.

In this work, we define the 'earthquake arrest zone' as a subsection of an earthquake's rupture area. It is bounded on one side by the tip of an arrested earthquake rupture. The boundary on the other side is not as clearly defined, but is roughly located where the stress changes that occur during the earthquake $\Delta\tau(x) > \Delta\tau_{min}$, as shown in Fig. 1(d). When a propagating rupture enters the earthquake arrest zone, the rupture front decelerates and ultimately arrests. The elliptical model has an earthquake arrest zone width $w_{az} = 0$, and the bell-shaped model has a finite w_{az} with constant stress changes within the arrest zone. In our experiments, we find w_{az} on each end of the rupture is approximately 20 per cent of the overall rupture length, and within each earthquake arrest zone we observe stress changes that gradually transition from a peak at the rupture tip to a minimum within the interior of the ruptured region. We propose an analytical crack model that accommodates the aforementioned observations and adheres to physical constraints better than previous models.

For each crack model, stress changes can be plotted against slip, as shown in Fig. 1(e). Our proposed model produces a relationship that, on first glance, appears to be similar to a linear slip weakening relationship (e.g. Ida 1972; Palmer & Rice 1973; Andrews 1976). However, Fig. 1(e) shows the final slip and static stress changes at many different locations throughout the earthquake arrest zone, and this is different from a linear slip weakening relationship which describes the evolution of frictional strength as a function of slip at one location on the fault. As will be shown in this work, the earthquake arrest zone is fundamentally different from the cohesive zone defined in fracture mechanics (e.g. Freund 1990; Day *et al.* 2005) due to its physical interpretation. The cohesive zone depends primarily on fault strength evolution (friction), but we will demonstrate that the earthquake arrest zone is produced by the heterogeneous initial stress distribution required to stop the earthquake rupture (see Section 6.3). Section 6.4 presents dynamic rupture simulations that confirm how arrest conditions affect the slip profile and static stress changes during an earthquake (and consequently, the $\Delta\tau$–δ relationships shown in Fig. 1e) but are largely independent of frictional strength.

The difference between a cohesive zone and an earthquake arrest zone has implications for how seismically observed earthquake fracture energy E_G should be interpreted. Here we draw a distinction between E_G—referred to simply as 'fracture energy' in seismology, or 'breakdown energy/work' in previous studies (Abercrombie & Rice 2005; Viesca & Garagash 2015; Cocco *et al.* 2016; Perry *et al.* 2020)—and Γ the fracture energy normally used in fracture mechanics (e.g. Andrews 1976; Day *et al.* 2005). Γ is a local property of the material or interface that depends on local strength evolution $\tau_s(\delta)$ according to $\Gamma = \int_0^\infty [\tau_s(\delta) - \tau_r]\, d\delta$ (Rice 1968; Ida 1972), in which τ_r is the residual strength. (Γ is a constant in our numerical simulations presented in Section 6.4 that employ linear slip weakening friction.) E_G is the total strain energy released during the earthquake minus the radiated energy E_R and the frictional work on the fault plane E_F (Kanamori & Rivera 2006). It has been assumed that E_G derived from properties of seismic waves can be related to the strength of the interface or intact rocks (e.g. Abercrombie & Rice 2005). However, we suggest that the estimation of E_G can be greatly affected by rupture and arrest properties and is largely independent of fault strength and Γ.

2 EXPERIMENTAL METHODS AND MEASUREMENTS

Experiments were conducted on a biaxial direct shear apparatus as shown in Fig. 2. Slip events occurred on the simulated fault as shear load increased. The dimensions of the moving block and the stationary block are 3.10 m × 0.81 m × 0.30 m, and 3.15 m × 0.61 m × 0.30 m (respectively) in the x-, y- and z-directions. The dimensions of the simulated fault are 3.10 m × 0.30 m with area $A = 0.95$ m^2. The fault surfaces of the granite samples were prepared by the manufacturer to be flat and parallel to 125 μm. Mechanical properties of the Barre Gray granite are $E = 30$ GPa and $\nu = 0.23$.

The normal loading array, consisting of 18 × 2 hydraulic cylinders, presses the two rock blocks together in the y-direction and

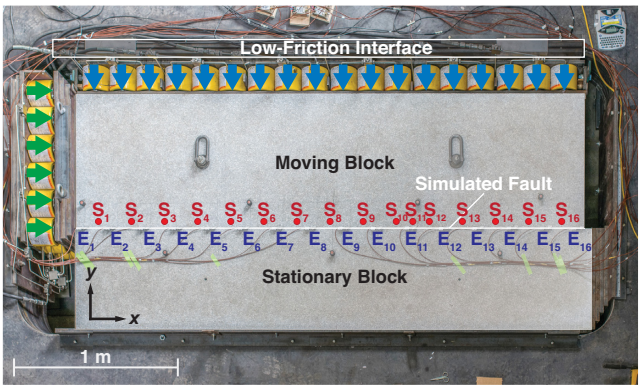

Figure 2. Experimental setup. The moving block and the stationary block were pressed together to compose the simulated fault of granite. A low friction interface consisted of a 2.4 mm thick sheet of reinforced Teflon sliding on precision ground steel plates ($\mu \approx 0.1$) allows the normal loading array (blue arrows) to translate with the moving block in the x-direction. The shear loading array (green arrows) pushes the moving block in the x-direction to apply shear stress and induce ruptures on the simulated fault. S_1–S_{16} show the locations of 16 sets of strain gauge pairs and E_1–E_{16} show the locations of 16 slip sensors.

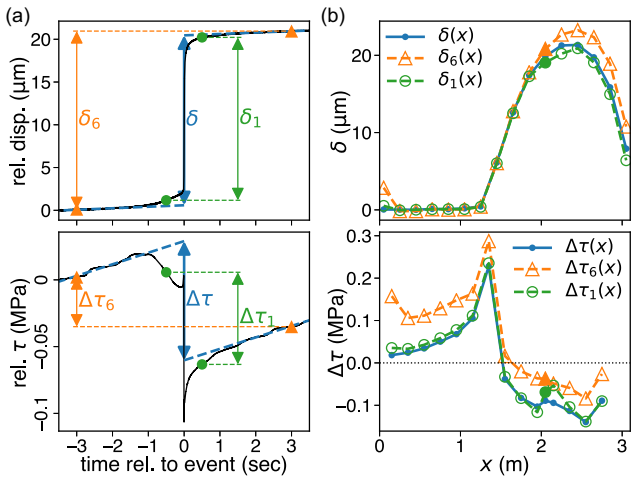

Figure 3. Example of slip and stress change time histories and extracted δ and $\Delta\tau$ from FS01–038–7MPa–P–1–03 event. (a) Heavy dashed lines are linear trends associated with continuous loading and fitted from data before ($t = -3$ to -2 s) and after ($t = 2$ to 3 s) the event. Parameters δ and $\Delta\tau$ are then defined by the difference between linear trends before and after the event extrapolated to the instant of dynamic rupture ($t = 0$) as shown. δ_6 and $\Delta\tau_6$ are defined by the difference with a 6-s time window, that is difference between $t = \pm 3$ s. Similarly, δ_1 and $\Delta\tau_1$ are defined by the difference with a 1-s time window. (b) Solid curves are results of $\delta(x)$ and $\Delta\tau(x)$ with linear trends removed. Dashed curves are estimates made without linear trends removed. The estimate from a 6-s window, $\delta_6(x)$, is slightly larger than $\delta_1(x)$ due to the inclusion of quasi-static slip during nucleation and after slip. Similarly, $\Delta\tau_6 > \Delta\tau_1(x)$ due to the inclusion of stress changes associated with continuous loading. Note that the deviations near $x = 2$ m in both $\delta_1(x)$ and $\Delta\tau_1(x)$ were due to the exclusion of the quasi-static nucleation process.

applies normal contact pressure on the fault. The shear loading array, consisting of 6 × 3 hydraulic cylinders, pushes the moving block in $+x$-direction and applies shear stress on the fault. Hydraulic cylinders in each array are interconnected to a manual pump, allowing us to independently control normal and shear loading. The measurements of hydraulic pressure in both arrays are then converted and reported as sample average normal and shear stress, $\bar{\sigma}$ and $\bar{\tau}$.

Local fault slip was measured by 16 evenly spaced eddy current displacement sensors at 16 locations (E_1–E_{16}) along the fault as shown in Fig. 2. These sensors measure the relative displacement between each side of the fault, that is the moving and the stationary rock blocks. Local shear strain was measured by 16 pairs (S_1–S_{16}) of semiconductor strain gauges at locations shown in Fig. 2, with S_{11} and E_{11} being collocated and all others evenly spaced between E_1–E_{16}. Each pair consists of two collocated 4 mm long semiconductor strain gauges oriented at 45° and 135° from the fault which were glued to the moving block, 5 mm from the fault. Local shear stress τ was derived from measurements of the strain gauge pair and the elastic properties of Barre Gray granite. While the 5 mm off-fault measurement can be biased for dynamic responses (Svetlizky & Fineberg 2014; Kammer & McLaskey 2019; Svetlizky *et al.* 2020), we assume negligible differences between on-fault and 5 mm off-fault measurements when at (quasi-)static stress states.

Before every experiment, we apply $\bar{\sigma} \approx 1$ MPa and then increase τ until the whole simulated fault slips a few times to create a consistent initial stress distribution for the following procedures. During the experiments, normal load was first increased to the prescribed level $\bar{\sigma}_0$ and a valve was closed to keep the volume of hydraulic fluid in the normal loading array constant. Shear load was then increased at a roughly constant rate to induce sequences of slip events. Further information about the experimental setup, procedures, and mechanics of the sequences can be found in Ke *et al.* (2018) and Wu & McLaskey (2019).

In this work, we study individual coseismic slip events. In our experiments, slow fault creep and nucleation-related slow slip sometimes occurs prior to and after slip events, as shown in Fig. 3(a). For these events, using a smaller time window to calculate δ and $\Delta\tau$ could exclude quasi-static nucleation process and result in incomplete $\delta(x)$ and $\Delta\tau(x)$, as shown in Fig. 3(b). On the other hand, using a larger time window that includes the nucleation process and afterslip will also include stress changes from the slow and continuous loading and slip from quasi-static steady slow slip. We account for these slow processes by fitting linear trends in time histories before and after the dynamic rupture process then extrapolating the linear time histories to the instant of the dynamic rupture process and we then take differences to define the δ and $\Delta\tau$ associated with a dynamic slip event from each location (Fig. 3). In our experiments, rapid afterslip appears to slightly decrease the stress increase at the rupture tip of arrested ruptures (not shown), and likely accounts for only a 5 per cent change. The above procedure lumps the slow slips prior to and after the dynamic rupture to the changes between the static states before and after the event. Events with fast nucleation and no afterslip are unaffected.

3 SPATIAL DISTRIBUTION OF STRESS CHANGES

For a mode II (in-plane shear) crack, we define the spatial distribution of shear stress change associated with an earthquake rupture as $\Delta\tau(x) \equiv \tau_f(x) - \tau_0(x)$, where $\tau_0(x)$ is the spatial distribution of shear stress at the (quasi-)static state before the rupture nucleates and $\tau_f(x)$ is the spatial distribution of shear stress at the (quasi-)static state after the rupture arrests. Thus, $\Delta\tau(x)$ is the shear stress changes due to all processes of a rupture (nucleation, dynamic rupture propagation and rapid afterslip) between two (quasi-)static states. Bilby & Eshelby (1968) derived the constitutive relationship between the

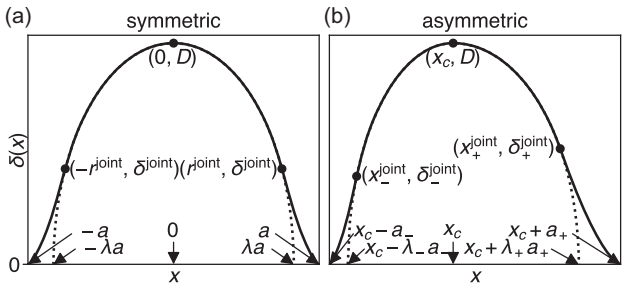

Figure 4. Parameters of the proposed slip profile model in one-dimensional (a) symmetric form (eq. 2) and (b) asymmetric form (eq. 3). (a) Dotted curve shows the elliptical model this model follows between $\pm r^{\text{joint}}$ with radius λa and height $\delta(0) = D$, in which a is the half-length of the rupture and $0 < \lambda < 1$. (b) Dotted curve shows the asymmetric elliptical model this model follows between $x_{\pm}^{\text{joint}}$ with radius $\lambda_{\pm}a_{\pm}$ on either side of x_c, in which x_c is the location such that $\delta(x_c) = D$, $x_c \pm a_{\pm}$ are the locations of rupture tips $x_{\pm}^{\text{tip}}$.

distribution of slip parallel to the fault $\delta(x)$ and shear stress change distribution $\Delta\tau(x)$,

$$\Delta\tau(x) = -\frac{\mu^*}{2\pi}\int_{a_-}^{a_+}\frac{d\delta(\xi)/d\xi}{x-\xi}d\xi, \tag{1}$$

where $\mu^* = \mu/(1-\nu)$ for mode I and II, $\mu^* = \mu$ for mode III, in which μ is the shear modulus and ν is the Poisson's ratio, and $a_{\pm}$ are the locations of the rupture tips. This equation assumes the material surrounding the rupture is linear elastic. It takes the first derivative of the slip profile $d\delta(x)/dx$ as input and gives its respective static stress change distribution $\Delta\tau(x)$. Note that if a given $\delta(x)$ is C^1 continuous and $\delta(x) \sim (\pm[a_{\pm} - x])^{3/2}$ as x approaches $a_{\pm}$ within the rupture, its respective $\Delta\tau(x)$ is smooth and finite (see Uenishi & Rice 2003: appendix A).

4 PROPOSED CRACK MODEL

Our model combines the elliptical shape in the centre of the rupture and an $r^{3/2}$ form at the edges, which replaces stress singularities in the elliptical model with mathematically simplistic earthquake arrest zones. The edges of the slip profile are approximately linear (Fig. 1a), consistent with slip profiles obtained from natural faults. The proposed analytical model of slip profiles is formulated as

$$\delta(r) = \begin{cases} D\left[1-\left(\frac{r}{\lambda a}\right)^2\right]^{1/2}, & 0 \le r \le r^{\text{joint}} \\ \delta^{\text{joint}}\left(\frac{r-a}{r^{\text{joint}}-a}\right)^{3/2}, & r^{\text{joint}} < r \le a \\ 0, & a < r \end{cases} \tag{2}$$

where r is the distance to the centre of the crack, a is the radius of the crack, λ scales a to the radius of the ellipse $a^{\text{ellipse}} = \lambda a$, in which $0 < \lambda < 1$, $r^{\text{joint}} = a\left(\sqrt{1+3\lambda^2}-1\right)$ is the radius where $\delta(r)$ switches between elliptical and $r^{3/2}$ form, and $\delta^{\text{joint}} = \delta(r^{\text{joint}})$, as shown in Fig. 4(a). Compared to the elliptical (or ellipsoidal) model, $\delta(r) = D\left[1-\left(\frac{r}{a}\right)^2\right]^{1/2}$ for $0 \le r \le a$, this model introduces only one additional parameter, λ, and guarantees C^1 continuity in $\delta(r)$ and no singularity in the associated stress changes if $0 < \lambda < 1$. Note that this model reduces into the elliptical model if $\lambda = 1$.

We extend the model to an asymmetrical formulation in a 1-D coordinate system (x) by introducing a new parameter x_c as the location of the maximum δ and repeating a and λ on either side of x_c,

$$\delta(x) = \begin{cases} \delta_-^{\text{joint}}\left(\frac{x - x_-^{\text{tip}}}{x_-^{\text{joint}} - x_-^{\text{tip}}}\right)^{3/2}, & x_-^{\text{tip}} < x < x_-^{\text{joint}} \\ D\left[1-\left(\frac{x-x_c}{\lambda_- a_-}\right)^2\right]^{1/2}, & x_-^{\text{joint}} \le x < 0 \\ D\left[1-\left(\frac{x-x_c}{\lambda_+ a_+}\right)^2\right]^{1/2}, & 0 \le x \le x_+^{\text{joint}} \\ \delta_+^{\text{joint}}\left(\frac{x_+^{\text{tip}} - x}{x_+^{\text{tip}} - x_+^{\text{joint}}}\right)^{3/2}, & x_+^{\text{joint}} < x < x_+^{\text{tip}} \\ 0, & \text{otherwise} \end{cases} \tag{3}$$

where x_c is the location of maximum δ such that $\delta(x_c) = D$, $a_{\pm}$ are the rupture half-lengths on either side of x_c, $x_{\pm}^{\text{tip}} = x_c \pm a_{\pm}$ are the locations of rupture tips, $\lambda_{\pm}$ controls the radius of the ellipse $a_{\pm}^{\text{ellipse}} = \lambda_{\pm}a_{\pm}$, in which $0 < \lambda_{\pm} < 1$, $x_{\pm}^{\text{joint}} = x_c \pm \left(\sqrt{1+3\lambda_{\pm}^2}-1\right)a_{\pm}$ are the locations where $\delta(x)$ switches between elliptical and $(\pm[a_{\pm} - x])^{3/2}$ forms, and $\delta_{\pm}^{\text{joint}} = \delta(x_{\pm}^{\text{joint}})$, as shown in Fig. 4(b).

5 RESULTS

Fig. 5 shows slip profiles and associated stress changes measured from eight different contained laboratory-generated earthquakes and the respective model fits, where events (1)–(4) are completely contained and events (5)–(8) are partially contained. The spatial resolution of slip profile $\delta(x)$ measurements is arguably not high enough to resolve the fine details near the rupture tips. However, $\Delta\tau(x)$ is very sensitive to the details of $\delta(x)$ non-locally, therefore measurements of $\Delta\tau(x)$ provide additional data to guide and resolve the fine details in $\delta(x)$ near the rupture tips. Simultaneously fitting a model to both $\delta(x)$ measurements and $\Delta\tau(x)$ measurements is a more robust way to resolve $\delta(x)$ and the associated $\Delta\tau(x)$ of earthquake ruptures compared to interpolating between sparse measurements.

Fig. 5(b) shows two relatively large rupture events (4) and (8) from our experiments to demonstrate the quality of model fits of the elliptical, the bell-shaped and the proposed models. To accommodate the restriction that the bell-shaped model cannot be stretched asymmetrically, we sliced slip profiles in half with respect to the location of maximum δ for the comparison between models. All three models fit $\delta(x)$ well, however, the shapes of $\Delta\tau(x)$ differ near the rupture tip, that is in the earthquake arrest zone. Importantly, our $\Delta\tau(x)$ measurements nearly always contain at least one data point with an intermediate value of $\Delta\tau$ located between the maximum $\Delta\tau$ at the rupture tip and the nearly constant $\Delta\tau$ within the central portion of the ruptured region. Even though the spatial resolution of strain measurements is not high enough to verify the exact shape of $\Delta\tau(x)$ within the earthquake arrest zone, they provide clear evidence of the existence of an earthquake arrest zone and a smoothly varying $\Delta\tau(x)$ within the arrest zone. The proposed model better matches our data then the discontinuity in $\Delta\tau(x)$, which is a feature of both the elliptical and the bell-shaped models. Of the 24 completely contained ruptures and 13 partially contained ruptures studied here, the coefficient of determination R^2 of $\delta(x)$ and $\Delta\tau(x)$ fits are 97.7 per cent $\pm$ 2.3 per cent and 83.7 per cent $\pm$ 10.7 per cent, respectively.

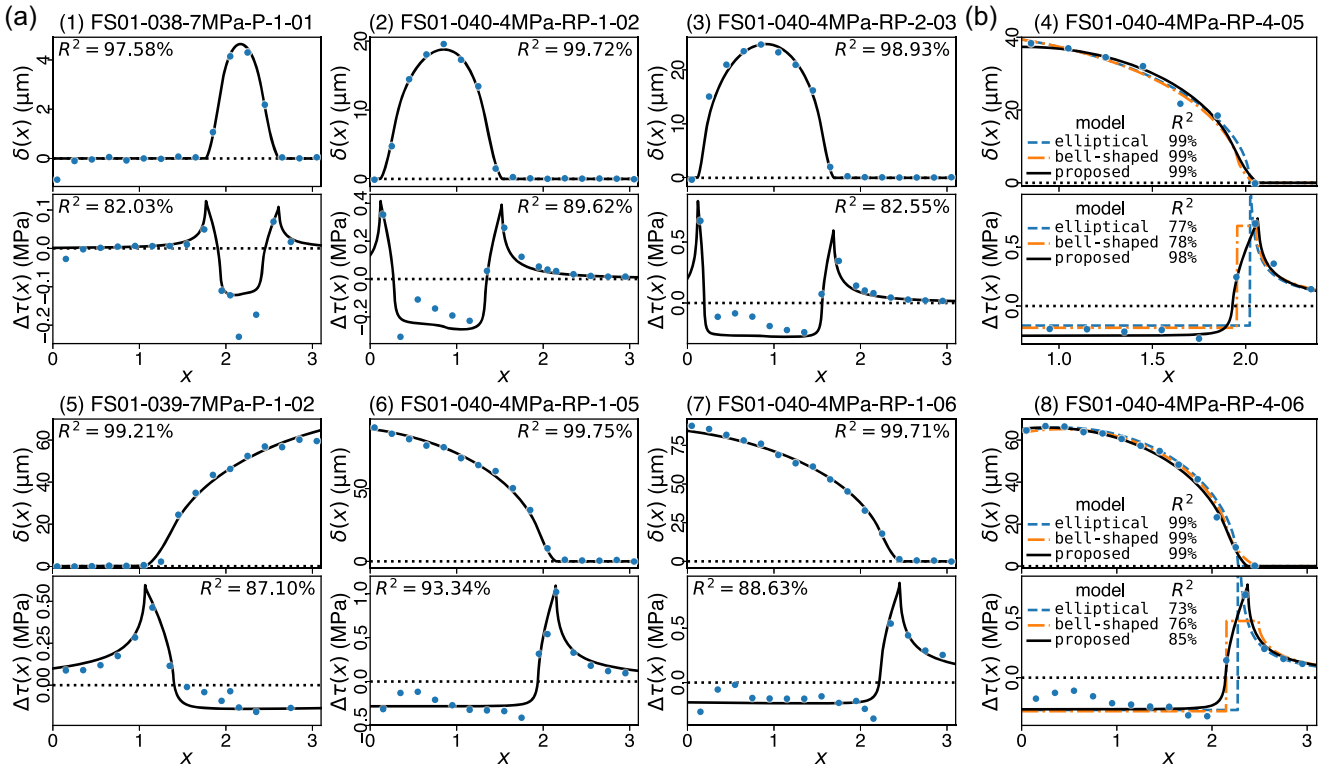

Figure 5. Examples of measured rupture events and model fits of (1)–(4) completely contained and (5)–(8) partially contained laboratory earthquakes. (a) Blue dots indicate measurements of $\delta(x)$ and $\Delta\tau(x)$. Solid curves are results of model fits. The coefficient of determination R^2 of model fits is marked next to each curve. (b) Comparison between the elliptical, the bell-shaped and the proposed models. Entries in legends denote R^2 of each model fit, where only half of the rupture is shown.

6 DISCUSSION

6.1 Earthquake arrest zone and comparison between different models

The proposed model merges an elliptical slip profile with a $x^{3/2}$ form at the edges. This allows constant stress drop in the centre while keeping the stress concentration at rupture tips finite, and retains a smooth transition in between. The linear tapering feature in slip profiles observed in natural faults is related to the existence of an earthquake arrest zone. Our model's earthquake arrest zone width is $w_{az} \equiv 2(a - r^{joint}) = 2a\left(2 - \sqrt{1+3\lambda^2}\right)$, as shown in the shaded area in Fig. 1(d). It is the region where $\delta(x)$ is approximately linear and where $\Delta\tau(x)$ transitions from the stress drop within the ruptured region, $\Delta\tau_{min}$, to the maximum stress increase at the tips of the arrested rupture, $\Delta\tau_{max}$. The earthquake arrest zone width w_{az} increases with rupture length $2a$ but their ratio $w_{az}/2a$ is a function of only the shape parameter λ, that is $w_{az}/2a = 2 - \sqrt{1+3\lambda^2}$. w_{az} vanishes if $\lambda = 1$ and widens as λ decreases.

The values of λ that best fit laboratory measurements of completely contained ruptures ranged from 0.49 to 0.99, with a median value of 0.85 which reflects $w_{az}/2a \approx 20$ per cent, consistent with field observations from larger earthquakes (Cowie & Scholz 1992; Scholz & Lawler 2004).

w_{az} in the proposed model is conceptually similar to the friction breakdown zone width of the bell-shaped model (s in Cowie & Scholz 1992, or $a - d$ in Bürgmann *et al.* 1994). In the Walsh & Watterson (1987) model, the earthquake arrest zone is essentially the entire rupture half-length. This model also has the approximately linear tapering feature at the edges and limited stress concentration at rupture tips, but its associate stress changes have a fixed triangular shape that does not match our observations or other models that show roughly uniform $\Delta\tau(x)$ inside the ruptured region.

6.2 Scaling of the earthquake arrest zone, earthquake stress drop and seismically observed earthquake fracture energy E_G

Our experiments produce contained ruptures with half-lengths that range from 0.5 to 2 m. By itself, this provides limited scaling information, and we observe no apparent trend in D or λ against rupture size. However, we gain important insights by imposing some physical constraints supported by field observations of large and small earthquakes.

Earthquake ruptures range in size from hundreds of km to hundreds of mm while absolute strength and fracture energy of the rocks (τ_p, τ_r, Γ) and stress levels of the crust (τ_0) should remain relatively scale independent. Note that the apparent peak stress $\Delta\tau_{max} + \tau_0(x)$ may not represent the actual peak strength of the interface τ_p. We expect $\Delta\tau_{max}$ to be bounded by $\tau_p - \tau_0(x)$. Therefore, $\Delta\tau_{max}$ should also be scale-independent with respect to rupture size. These constraints agree with the most physically reasonable of the scaling scenarios considered by Cowie & Scholz (1992). We also assume that the average stress drop during an earthquake $\overline{\Delta\tau} \propto \mu D/a$ is scale independent, consistent with observations of large and small earthquakes (e.g. Kanamori & Anderson 1975; Hanks 1977; Baltay *et al.* 2011).

To illustrate the scaling mathematically, we analytically calculate $\Delta\tau_{max}$ and $\Delta\tau_{min}$ by plugging the slip profile into eq. (1) at the

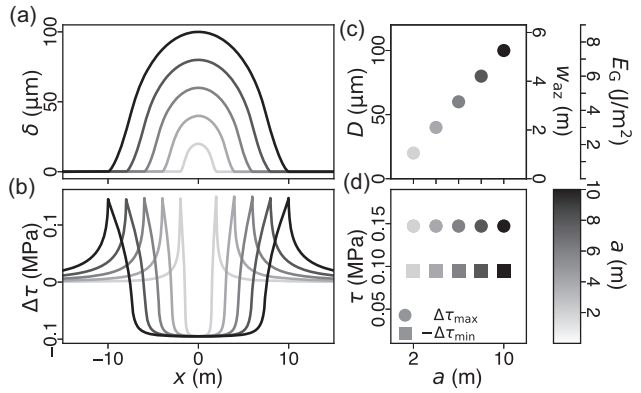

Figure 6. Scaling relations of the proposed model for a from 2 to 10 m. (a) Slip profile $\delta(x)$ of earthquake ruptures of different a and (b) the respective associated stress changes $\Delta\tau(x)$. (c) Scaling relations of maximum slip D, earthquake arrest zone width w_{az}, and seismically observed earthquake fracture energy E_G to a. (d) $\Delta\tau_{max}$ and $-\Delta\tau_{min}$ of different a.

rupture tip and at the centre. Assuming a symmetric crack, this results in

$$\Delta\tau_{max} = \Delta\tau(r = a) = \frac{\mu^*}{2\pi}\frac{D}{a}\Lambda_p(\lambda), \tag{4}$$

$$\Delta\tau_{min} = \Delta\tau(r = 0) = -\frac{\mu^*}{2\pi}\frac{D}{a}\Lambda_r(\lambda), \tag{5}$$

in which

$$\Lambda_p(\lambda) = -2\frac{\theta}{\lambda} + \frac{3\cos\theta}{\alpha^3}\left[2\alpha - \sqrt{2}\tanh^{-1}\left(\frac{\alpha}{\sqrt{2}}\right)\right] + \frac{2}{\lambda\beta}\left[\tan^{-1}\left(\frac{\lambda+\gamma}{\beta}\right) - \tan^{-1}\left(\frac{\lambda-\gamma}{\beta}\right)\right], \tag{6}$$

$$\Lambda_r(\lambda) = 2\frac{\theta}{\lambda} + \frac{6\cos\theta}{\alpha^3}\left[\tanh^{-1}(\alpha) - \alpha\right], \tag{7}$$

where $\alpha = \sqrt{1-\lambda\sin\theta}$, $\beta = \sqrt{1-\lambda^2}$, $\gamma = \tan(\theta/2)$ and $\theta = \sin^{-1}\left((\sqrt{1+3\lambda^2}-1)/\lambda\right)$. Namely, both $\Delta\tau_{max}$ and $\Delta\tau_{min}$ are proportional to μ^* and D/a. The stress ratio $\Delta\tau_{max}/(-\Delta\tau_{min}) = \Lambda_p(\lambda)/\Lambda_r(\lambda)$ spans $(0, +\infty)$ for $\lambda \in (0, 1)$, monotonically increases as λ increases, and monotonically decreases as $w_{az}/2a$ increases. This shows that the proposed model can adapt to arbitrary $\Delta\tau_{max}$ and $\Delta\tau_{min}$ as long as $\Delta\tau_{max} > 0 > \Delta\tau_{min}$, but might have limitations fitting both arbitrary stress ratio and arbitrary w_{az} since both depend on λ.

Imposing all the above constraints (scale independent D/a, $\Delta\tau_{max}$, $\Delta\tau_{min}$ and τ_0) necessitates a scale invariant λ, which describes a self-similar slip profile, as shown in Fig. 6(a). Note that Fig. 6 shows the scaling relations of independent arrested earthquake ruptures rather than snapshots of rupture growth. A result of self-similarity is that w_{az} scales with rupture length ($2a$), as shown in Fig. 6(c), and this implies that the seismically observed earthquake fracture energy E_G increases with earthquake size, consistent with seismic observations (Abercrombie & Rice 2005). In our model with constant λ, $E_G \propto \delta^{joint} \propto D$. Since D/a is also a constant, $E_G \propto a$. Note also that $E_G \propto w_{az}$ since both $w_{az} \propto a$ and $E_G \propto a$, for fixed λ.

The scaling relations described above are not unique to our proposed model; they are identical to those proposed for the bell-shaped model (Cowie & Scholz 1992) and similar to a recent theoretical model of dynamic ruptures (Weng & Ampuero 2019). The self-similar scaling is also consistent with the CFTT (constant fault tip taper) model (Scholz & Lawler 2004; Scholz 2019), analogous to constant CTOA (crack tip opening angle) model for mode I fracture (Kanninen & Popelar 1985). Since our proposed model has a slip profile that is fairly close to a linear taper, we propose that it can be considered a first-order analytical approximation to the CFTT model.

6.3 Physical mechanisms underlying fault tip taper and earthquake arrest zone

Field evidence shows that fault tip taper increases with stress at the rupture tip (Scholz & Lawler 2004). As a result, earthquakes that rupture a preexisting fault (with lower strength) taper more gradually than shear cracks that form new faults. This relationship can be derived analytically from our proposed model. We define that the fault tip taper

$$\mathrm{FTT} \equiv \frac{\delta^{joint}}{w_{az}/2} = \frac{D}{a}\frac{\cos\theta}{(1-\lambda\sin\theta)} \equiv \frac{D}{a}F(\lambda), \tag{8}$$

where $\delta^{joint} = D\cos\theta$, $\theta = \sin^{-1}\left((\sqrt{1+3\lambda^2}-1)/\lambda\right)$, and F is a monotonically increasing function of λ. If λ is constant, the maximum stress change, the minimum stress change, and their difference scales positively with FTT since FTT, $\Delta\tau_{max}$, and $\Delta\tau_{min}$ are all proportional to D/a.

The linear taper of the slip profile has been thought to be due to inelastic deformation in the rock volume around the fault tips (Cowie & Scholz 1992; Bürgmann *et al.* 1994; Scholz & Lawler 2004) possibly over multiple earthquake ruptures (Walsh & Watterson 1987). However, our laboratory earthquake ruptures exhibit earthquake arrest zones but show no sign of off-fault damage, suggesting that the features observed in the earthquake arrest zone can result from either friction processes occurring at the interface, or some other mechanisms.

The approximately linear taper at the edges of $\delta(x)$ and, equivalently, the earthquake arrest zone observed from $\Delta\tau(x)$ measurements in our experiments is orders of magnitude larger than the length-scale of cohesive zones that result from commonly used friction laws, for example slip-weakening friction (Ida 1972; Palmer & Rice 1973; Andrews 1976) and rate- and state-dependent friction (Dieterich 1979; Ruina 1983), which also exhibit slip-weakening behaviour during dynamic rupture propagation (Cocco & Bizzarri 2002). While the averaged w_{az} of completely contained rupture events from our experiments was about 0.4 m, fracture mechanics theory (Palmer & Rice 1973) predicts a cohesive zone width of $w_{coh} = 9\pi K^2/[32(\tau_p - \tau_r)^2] = 9\pi E d_0^2/(128\Gamma) \approx 10$ mm with $\Gamma \approx 1$ J m^{-2} (Kammer & McLaskey 2019) and $d_0 = 1\,\mu$m, which is reasonable for the bare granite surfaces in our experiment. The 5 mm off-fault location of the strain gauges cannot explain this discrepancy. Furthermore, past experiments where both the top and bottom surfaces of the granite sample were instrumented with slip sensors showed that ruptures were generally one-directional, so it is unlikely that 2-D effects associated with the 0.3 m thickness of the granite sample strongly affect our estimates.

We argue that the earthquake arrest zone observed in our experiments and the corresponding linear taper that has been mapped in field studies are primarily the result of a heterogeneous initial stress $\tau_0(x)$ prior to rupture and does not relate directly to the strength evolution of the interface. Under uniform stress, strength, and fracture energy Γ, fracture mechanics predicts that crack growth will not slow down once it initiates. Therefore, in order to stop an earthquake rupture, the rupture front must encounter either a barrier with high fracture energy $\Gamma(x)$ or unfavourable stress conditions, that is

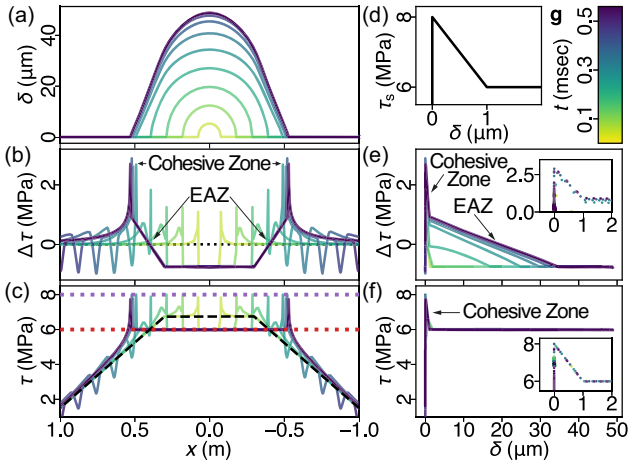

Figure 7. Dynamic simulation of an initial shear stress distribution $\tau_0(x)$ that results in linear slip taper. (a) Snapshots of the slip profile $\delta(x)$, (b) the respective associated stress changes $\Delta\tau(x)$, and (c) the respective absolute stress $\tau(x)$ of the dynamic rupture at different times colour coded with (g), in which the opaque dark blue curves represent the static outcomes. Black dashed line in (c) shows a trapezoidal initial stress distribution $\tau_0(x)$. Purple and red dotted lines show the peak strength and the residual strength levels. Oscillations in both (b) and (c) are the shear wave emitted from the nucleation. (d) Depicts the imposed strength evolution law $\tau_s(\delta)$. (e) and (f) show the resultant $\Delta\tau$–δ and τ–δ relationships at different times, respectively. Insets are zoomed-in at the spike near $\delta = 0$. The inset in (f) strictly follows $\tau_s(\delta)$ shown in (d). The extent of linear slip taper in (a) coincides with the linear transition from $\Delta\tau_{min}$ to $\Delta\tau_{max}$ in (b).

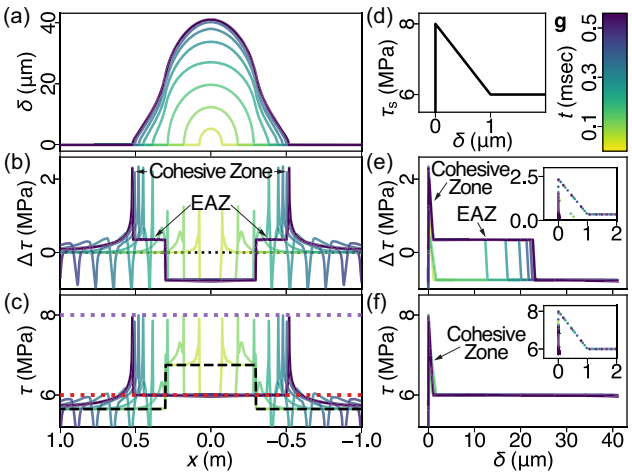

Figure 8. Dynamic simulation of an initial shear stress distribution $\tau_0(x)$ that results in a bell-shaped slip profile. All panels are similar to Fig. 7. Black dashed line in (c) shows a boxcar initial stress distribution $\tau_0(x)$. Note that $\tau_0(x) < \tau_r$ outside the boxcar.

$\tau_0(x) < \tau_r$. Even though previous studies (e.g. Abercrombie & Rice 2005; Viesca & Garagash 2015; Cocco *et al.* 2016; Nielsen *et al.* 2016) have reported scale-dependent 'earthquake fracture energy' E_G, $\Gamma(x)$ is considered a scale-independent material or interfacial property (e.g. Day *et al.* 2005). We believe that the most likely reason for rupture termination is propagation into unfavourable stress conditions, at least for earthquakes rupturing preexisting faults (Ke et al., 2018). This is similar to the idea of rupture interacting with the stress shadow of a previous earthquake on the same fault (e.g. Gupta & Scholz 2000). As illustrated by the dynamic rupture simulations described in Section 6.4, we suggest that the $\Delta\tau(x)$ in the earthquake arrest zone, the $\Delta\tau$–δ relations of Fig. 1(e), and the corresponding linear taper in $\delta(x)$ are the result of rupture termination conditions and bear little resemblance to the underlying friction behaviour of the material or interface. The stress changes within the earthquake arrest zone $\Delta\tau(x)$ mainly reflect the transition of $\tau_0(x)$ from above to below τ_r. Large earthquakes appear to have large w_{az} and large seismically observed fracture energy E_G because they must propagate further into unfavourable stress conditions to halt rupture. It is possible that the scale dependency of E_G could result from the scale-dependent earthquake arrest zone while Γ remains scale-independent.

6.4 Examples of heterogeneous $\tau_0(x)$ as the source of observed earthquake arrest zone features

To test the above conjecture that the seismically inferred $\Delta\tau$–δ relationship can be the result of heterogeneous $\tau_0(x)$, we simulated fully dynamic rupture propagation and termination with the spectral boundary integral method (Breitenfeld & Geubelle 1998) in two different initial stress distributions $\tau_0(x)$. The first example (Fig. 7) has a trapezoidal $\tau_0(x)$, shown as the black dashed line in Fig. 7(c), and the resulting slip distribution and stress changes emulate the features of the earthquake arrest zone that we observed in the laboratory experiments. The second example (Fig. 8) has a boxcar $\tau_0(x)$, shown as the black dashed line in Fig. 8(c), to emulate the earthquake arrest zone with a constant stress change. Both simulations have identical material properties ($E = 30$ GPa, $\nu = 0.23$, $\rho = 2700\ \mathrm{kg\,m^{-3}}$) and linear slip-weakening strength evolution law $\tau_s(\delta)$ with peak strength $\tau_p = 8$ MPa, residual strength $\tau_r = 6$ MPa, and critical slip distance $d_0 = 1\ \mu$m. The dynamic rupture is nucleated by manually extending a seed crack (dropping τ_p to τ_r) bilaterally from $x = 0$ at half the Rayleigh wave speed until it reaches the critical crack length $L_c \approx 36$ mm and becomes unstable spontaneously. The rupture front then accelerates towards the Rayleigh wave speed and decelerates once it propagates into unfavourable stress states, that is $\tau_0(x) < \tau_r(x)$. When the rupture runs out of available strain energy to release, it spontaneously arrests.

The difference between Figs 7(e) and (f), and similarly between Figs 8(e) and (f), demonstrates the distinction between the $\Delta\tau$–δ that can be inferred from earthquake observations and the underlying frictional strength evolution τ_s–δ relationship. Since the absolute stress level τ in the Earth is mainly inaccessible, the measured or inferred $\Delta\tau$ from earthquakes was sometimes thought to represent the absolute stress level by assuming $\tau_0(x)$ is uniform across the extent of a rupture. With these two examples, we demonstrated that the apparent features in $\delta(x)$, such as linear taper or bell-shaped, and in $\Delta\tau$, such as smooth transition or a sudden step, can solely result from the shape of the initial stress distribution $\tau_0(x)$. While the actual cohesive zone is small and hard to measure, the apparent large-scale feature of $\Delta\tau(x)$ in the arrest zone (Fig. 7b) and the apparent slip-weakening feature in the $\Delta\tau$–δ curve (Fig. 7e) can be produced by the heterogeneous $\tau_0(x)$ and the misrepresentation of $\Delta\tau$ as τ_s. Similarly, with a crafted $\tau_0(x)$ (Fig. 8c), we can emulate a bell-shaped slip profile (Fig. 8a) with linear elasticity (and no off-fault damage).

6.5 Smooth observed slip profile

Our contained laboratory-generated earthquakes have smoother slip profiles compared to natural earthquakes. This could be because the simulated fault is more smooth and flat than natural faults. Another

possibility is that our experiments produced 'baby' earthquakes that reached unfavourable stress conditions and terminated soon after nucleating and before the rupture front was fully dynamic (Svetlizky *et al.* 2017), and therefore more complex high-speed processes could not engage. Measurements of $\Delta\tau(x)$ inside the ruptured region, where dynamic rupture propagation took place, were slightly more deviated from the model and less smooth compared to the rest of the fault, as shown in Fig. 5. Perhaps the ruptures are not completely homogeneous along depth while the strain gauges are glued on the surface of the rock blocks, or some randomness is introduced by the rapid fluctuations in slip and stress during the dynamic rupture process as seen in a previous study with a similar experimental setup (McLaskey *et al.* 2015).

7 CONCLUSIONS

Our contained laboratory-generated earthquakes ruptured a nominally flat and smooth frictional interface free from heterogeneities in geometry and material properties. We found that heterogeneity in initial stress distribution was sufficient to generate laboratory earthquakes that terminated within the 3-m long simulated fault, providing a rare opportunity to study the features of slip profiles and the associated stress changes in a simplified laboratory setting. In addition to local slip measurements, we used local shear strain measurements to help resolve the details of slip profiles near the rupture tips, where stress changes are profound. Near the rupture tips, we consistently observe an earthquake arrest zone where stress changes smoothly transition from the maximum level at the crack tip to the minimum level within the ruptured region. The earthquake arrest zone was 0.06–0.95 m in size and was, on average, about 20 per cent of the overall rupture length, consistent with field observations of constant slip gradients (Cowie & Scholz 1992; Scholz & Lawler 2004). However the size of the arrest zone we observe is orders of magnitude larger than the cohesive zone predicted by fracture mechanics theory, using reasonable values of friction parameters. This leads us to believe that the observed features in the arrest zone are primarily produced by the heterogeneous initial stress distribution required to stop an earthquake rupture rather than the fault strength. Using a set of numerical simulations of spontaneous dynamic rupture propagation and termination, we illustrated how an earthquake's stress change versus slip relationship ($\Delta\tau$–δ) inferred from static stress changes can be profoundly different from the underlying frictional strength evolution (τ_s–δ). This has profound implications for how seismically derived estimates of certain earthquake parameters should be interpreted: the seismically inferred increase in fracture energy E_G and critical slip distance d_0 with increasing earthquake size (e.g. Abercrombie & Rice 2005) reflects the manner in which earthquake ruptures arrest rather than the way fault strength evolves with slip.

We propose a slip profile model that does not contain the stress singularity of the elliptical model; it has an earthquake arrest zone that moderates stress changes at the rupture tip. Different from previous models that also include an earthquake arrest zone, such as the bell-shaped model (Cowie & Scholz 1992; Bürgmann *et al.* 1994), our proposed model features smoothly varying stress changes that are more compatible with our laboratory measurements, and this facilitates the interpretation of the extent of the earthquake arrest zone that is otherwise difficult to define. While the full details of the stress changes within the earthquake arrest zone are not resolved due to limited spatial resolution in our experimental measurements, the inferred model provides a proper first-order approximation to the smooth transition from the maximum to the minimum level through a mathematically simple and numerically stable formulation of the slip profile. Constrained by physical measurements, the model may be useful as a component of more complicated fault rupture and rupture sequence earthquake models.

ACKNOWLEDGEMENTS

This research was supported by the National Science Foundation under grant EAR-1763499. Data used in this paper were acquired during laboratory experiments conducted at Cornell University. Data reported here are publicly available at https://eCommons.cornell.edu. We thank C. Scholz for a helpful review that stimulated transformative changes to this paper. We thank H. Weng, and two anonymous reviewers for their helpful reviews. We thank Bill S. Wu for assistance with the experiments. The authors declare that they have no conflict of interest.

REFERENCES

Abercrombie, R.E. & Rice, J.R., 2005. Can observations of earthquake scaling constrain slip weakening? *Geophys. J. Int.,* **162**(2), 406–424.

Andrews, D.J., 1976. Rupture propagation with finite stress in antiplane strain, *J. geophys. Res.,* **81**(20), 3575–3582.

Baltay, A., Ide, S., Prieto, G. & Beroza, G., 2011. Variability in earthquake stress drop and apparent stress, *Geophys. Res. Lett.,* **38**(6), 1–6.

Bilby, B.A. & Eshelby, J.D., 1968. Dislocations and the theory of fracture, in *Fracture, an Advanced Treatise, Vol. I, chap. 2,* pp. 99–182, ed. Liebowitz, H., Academic, San Diego, CA.

Breitenfeld, M.S. & Geubelle, P.H., 1998. Numerical analysis of dynamic debonding under 2D in-plane and 3D loading, *Int. J. Fract.,* **93**(1/4), 13–38.

Bürgmann, R., Pollard, D.D. & Martel, S.J., 1994. Slip distributions on faults: effects of stress gradients, inelastic deformation, heterogeneous host-rock stiffness, and fault interaction, *J. Struct. Geol.,* **16**(12), 1675–1690.

Cocco, M. & Bizzarri, A., 2002. On the slip-weakening behavior of rate- and state dependent constitutive laws, *Geophys. Res. Lett.,* **29**(11), 11–1-11-4, doi:10.1029/2001GL013999.

Cocco, M., Tinti, E. & Cirella, A., 2016. On the scale dependence of earthquake stress drop, *J. Seismol.,* **20**(4), 1151–1170.

Cowie, P.A. & Scholz, C.H., 1992. Physical explanation for the displacement-length relationship of faults using a post-yield fracture mechanics model, *J. Struct. Geol.,* **14**(10), 1133–1148.

Dawers, N.H., Anders, M.H. & Scholz, C.H., 1993. Growth of normal faults: Displacement-length scaling, *Geology,* **21**(12), 1107.

Day, S.M., Dalguer, L.A., Lapusta, N. & Liu, Y., 2005. Comparison of finite difference and boundary integral solutions to three-dimensional spontaneous rupture, *J. geophys. Res.: Solid Earth,* **110**(12), 1–23.

Dieterich, J.H., 1979. Modeling of rock friction: 1. Experimental results and constitutive equations, *J. geophys. Res.,* **84**(B5), 2161.

Dudgale, D., 1960. Yielding of steel sheets containing slits, *J. Mech. Phys. Solids,* **8**(2), 100–104.

Freed, A.M., 2005. Earthquake triggering by static, dynamic, and postseismic stress transfer, *Annu. Rev. Earth Planet. Sci.,* **33**(1), 335–367.

Freund, L.B., 1990. *Dynamic Fracture Mechanics,* Vol. **25,** Cambridge University Press, Cambridge.

Gupta, A. & Scholz, C.H., 2000. A model of normal fault interaction based on observations and theory, *J. Struct. Geol.,* **22**(7), 865–879.

Hanks, T.C., 1977. Earthquake stress drops, ambient tectonic stresses and stresses that drive plate motions., *Pure appl. geophys.: Pageoph.,* **115**(1–2), 441–458.

Ida, Y., 1972. Cohesive force across the tip of a longitudinal-shear crack and Griffith's specific surface energy, *J. geophys. Res.,* **77**(20), 3796–3805.

Kammer, D.S. & McLaskey, G.C., 2019. Fracture energy estimates from large-scale laboratory earthquakes, *Earth planet. Sci. Lett.,* **511,** 36–43.

Kanamori, H. & Rivera, L., 2006. Energy partitioning during an earthquake, *Geophys. Monogr. Ser.,* **170,** 3–13.

Kanamori, H. & Anderson, D.L., 1975. Theoretical basis of some empirical relations in seismology, *Bull. seism. Soc. Am.,* **65**(5), 1073–1095.

Kanninen, M.F. & Popelar, C.H., 1985. *Advanced Fracture Mechanics,* Oxford University Press.

Ke, C.-Y., McLaskey, G.C. & Kammer, D.S., 2018. Rupture termination in laboratory-generated earthquakes, *Geophys. Res. Lett.,* **45**(23), 12784–12792.

Manighetti, I., King, G.C.P., Gaudemer, Y., Scholz, C.H. & Doubre, C., 2001. Slip accumulation and lateral propagation of active normal faults in Afar, *J. geophys. Res.: Solid Earth,* **106**(B7), 13667–13696.

Manighetti, I., Campillo, M., Sammis, C., Mai, P.M. & King, G., 2005. Evidence for self-similar, triangular slip distributions on earthquakes: Implications for earthquake and fault mechanics, *J. geophys. Res.,* **110**(B5), B05302, doi:10.1029/2004JB003174.

McLaskey, G.C., 2019. Earthquake initiation from laboratory observations and implications for foreshocks, *J. geophys. Res.: Solid Earth,* **124**(12), 12882–12904.

McLaskey, G.C., Kilgore, B.D. & Beeler, N.M., 2015. Slip-pulse rupture behavior on a 2 m granite fault, *Geophys. Res. Lett.,* **42**(17), 7039–7045.

Muraoka, H. & Kamata, H., 1983. Displacement distribution along minor fault traces, *J. Struct. Geol.,* **5**(5), 483–495.

Nicol, A., Watterson, J., Walsh, J.J. & Childs, C., 1996. The shapes, major axis orientations and displacement patterns of fault surfaces, *J. Struct. Geol.,* **18**(2–3), 235–248.

Nielsen, S., Spagnuolo, E., Smith, S.A., Violay, M., Di Toro, G. & Bistacchi, A., 2016. Scaling in natural and laboratory earthquakes, *Geophys. Res. Lett.,* **43**(4), 1504–1510.

Palmer, A.C. & Rice, J.R., 1973. The growth of slip surfaces in the progressive failure of over-consolidated clay, *Proc. R. Soc. A: Math. Phys. Eng. Sci.,* **332**(1591), 527–548.

Perry, S.M., Lambert, V. & Lapusta, N., 2020. Nearly magnitude-invariant stress drops in simulated crack-like earthquake sequences on rate-and-state faults with thermal pressurization of pore fluids, *J. geophys. Res.: Solid Earth,* **125**(3), doi:10.1029/2019JB018597.

Rice, J.R., 1968. A path independent integral and the approximate analysis of strain concentration by notches and cracks, *J. Appl. Mech.,* **35**(2), 379–386.

Ruina, A., 1983. Slip instability and state variable friction laws, *J. geophys. Res.: Solid Earth,* **88**(B12), 10359–10370.

Scholz, C.H., 2019. *The Mechanics of Earthquakes and Faulting,* 3rd edn. Cambridge University Press.

Scholz, C.H. & Lawler, T.M., 2004. Slip tapers at the tips of faults and earthquake ruptures, *Geophys. Res. Lett.,* **31**(21), 1–4.

Svetlizky, I. & Fineberg, J., 2014. Classical shear cracks drive the onset of dry frictional motion, *Nature,* **509**(7499), 205–208.

Svetlizky, I., Kammer, D.S., Bayart, E., Cohen, G. & Fineberg, J., 2017. Brittle fracture theory predicts the equation of motion of frictional rupture fronts, *Phys. Rev. Lett.,* **118**(12), 125501.

Svetlizky, I., Albertini, G., Cohen, G., Kammer, D.S. & Fineberg, J., 2020. Dynamic fields at the tip of sub-Rayleigh and supershear frictional rupture fronts, *J. Mech. Phys. Solids,* **137,** 103826.

Uenishi, K. & Rice, J.R., 2003. Universal nucleation length for slip-weakening rupture instability under nonuniform fault loading, *J. geophys. Res.: Solid Earth,* **108**(B1), 2042.

Viesca, R.C. & Garagash, D.I., 2015. Ubiquitous weakening of faults due to thermal pressurization, *Nat. Geosci.,* **8**(11), 875–879.

Walsh, J.J. & Watterson, J., 1987. Distributions of cumulative displacement and seismic slip on a single normal fault surface, *J. Struct. Geol.,* **9**(8), 1039–1046.

Weng, H. & Ampuero, J.P., 2019. The dynamics of elongated earthquake ruptures, *J. geophys. Res.: Solid Earth,* **124**(8), 8584–8610.

Wu, B.S. & McLaskey, G.C., 2019. Contained laboratory earthquakes ranging from slow to fast, *J. geophys. Res.: Solid Earth,* **108**(B1), 2019JB017865.